Analysis of optical dispersion parameters and electrochromic properties of manganese-doped Co_3O_4 dendrite structured thin films

R. Venkatesh[1], C. Ravi Dhas[1*], R. Sivakumar[2], T. Dhandayuthapani[2], P. Sudhagar[3], C. Sanjeeviraja[4], A. Moses Ezhil Raj[5],

[1]PG & Research Department of Physics, Bishop Heber College (Autonomous), Tiruchirappalli 620 017, India.

[2] Department of Physics, Alagappa University, Karaikudi 630 004, India.

[3]Photocatalyst and Coatings Group, SPECIFIC, College of Engineering, Swansea University (Bay Campus), Fabianway, Swansea SA18EN, United Kingdom

[4]Department of Physics, Alagappa Chettiar College of Engineering & Technology, Karaikudi-630 004, India.

[5]Department of Physics, Scott Christian College, (Autonomous), Nagercoil 629 003, India.

Corresponding author address:

Dr. C. Ravi Dhas,

Head & Assistant Professor,

PG & Research Department of Physics,

Bishop Heber College (Autonomous),

Tiruchirappalli - 620 017,

Tamil Nadu, India.

Mobile: +91 9443076209

Land line: 0431- 2770136

Fax: 0431 – 2770293

e-mail id: ravidhasc@gmail.com (C. Ravi Dhas)

cravidhas@gmail.com

Analysis of optical dispersion parameters and electrochromic properties of manganese-doped Co_3O_4 dendrite structured thin films

Abstract

Nebulized spray pyrolysis method was employed to deposit pristine and manganese (Mn) -doped Co_3O_4 thin films for different Mn concentrations (4, 6 and 8 at.%). The structural properties revealed that the obtained films show predominant orientation along (311) plane and significant peak shift was observed upon an increase in Mn doping confirms the substitution of Mn in Co_3O_4 lattice. The pristine Co_3O_4 film shows clustered grains and dendrite patterns appearing with the increase in Mn content as evident from SEM studies. The optical dispersion parameters of the prepared films of pristine and Mn doped Co_3O_4 films were determined from UV transmission spectra. The phase purity and elemental analysis of the films revealed single phase with better stoichiometric films were obtained. The XPS core level spectra of 6 at.% Mn doped Co_3O_4 films exhibited the presence of two different oxidation states (Mn^{2+} and Mn^{3+}). The electrical resistivity of the films decreased with increase in Mn dopant concentration was observed from linear four probe method. The Co_3O_4 film deposited using 6 at.% of Mn exhibited a maximum optical modulation of 35 % and coloration efficiency of 29 cm^2/C.

Keywords: Oxides, Thin films, Microstructure, Electrochemical properties.

1. Introduction

The electrochromic phenomenon has attracted much attention as an intensive research area in the field of material science which has a remarkable ability to offer better output with less energy consumption. An electrochromic material should possess the following properties: high color contrast ratio, good memory effect and should be operated under low voltage [1]. Semiconducting transition metal oxides such as WO_3, MoO_3, V_2O_5, Co_3O_4, MnO_2, and Nb_2O_5 are the most explored materials for electrochromic applications [2]. Among them, WO_3 is the most extensively studied owing to its high electrochemical properties, but, it can provide a complementary blue color upon charge insertion and become transparent after extraction. At present electrochromic compounds exhibiting different colors needs to be focused as they are more feasible for replacing LED and LCD technologies which consume more electricity. In this aspect, Cobalt oxides (Co_3O_4, Co_2O_3 and CoO) and manganese oxides (MnO_2, Mn_3O_4 and MnO) are of particular interest owing to their excellent physiochemical properties. Co_3O_4 is a p-type semiconductor that crystallizes in spinel cubic form (Fd3m) and has shown high electrochemical activity and can be efficiently altered from brown to yellow color during intercalation of OH^- ions [3].

Manganese (Mn) can be used as a dopant ([Ar] $3d^5$ $4s^2$) that might effectively replace Co ([Ar] $3d^7$ $4s^2$) lattice sites and tailor the optical and electronic properties of Co_3O_4. Few research efforts have been made by substituting Mn in Co_3O_4 nanoparticles that delivered better functionality as an electrocatalyst in supercapacitors, anode material in lithium ion batteries, biosensors and oxygen reduction reactions (ORR) [4-7]. The interesting results obtained from the above-mentioned literature inspired us to understand the fundamental physics behind Mn-doped

Co_3O_4 system. Nanostructures in low dimensions especially in thin film form would be more attractive and capable of inducing more electrocatalytic active sites which reduce the ion diffusion paths at the film surface/electrolyte interface. The study of optical dispersion parameters becomes immensely important to design suitable electrochromic devices consisting of cathodic/anodic coloration compounds [8]. At present there are no reports available regarding the detailed discussion on the optical parameters of Mn-doped Co_3O_4 thin films.

Nebulized spray pyrolysis is more efficient and its simple engineering design has remarkable capacity to convert the precursor solution into fine smog like particles to yield device quality films compared to other sophisticated vacuum techniques and chemical solution methods [9, 10]. A wide variety of nanostructured thin films can be produced by nebulizer-assisted spray pyrolysis which is its prime advantage over conventional spray route. Keeping all these aspects in mind we are the first to report the effect of Mn doping concentration on the properties of Co_3O_4 thin films deposited on microscopic glass and FTO substrates using nebulizer spray technique. The structural, optical, electrical and electrochromic performance of the deposited films was investigated in detail.

2. Experimental details

2.1 Preparation of pristine and Mn-doped Co_3O_4 films

All the chemicals procured for this present work were of analytical grade and used as received without any further purification. Nebulized spray deposition (NSD) technique was employed to deposit Co_3O_4 and Mn-doped Co_3O_4 thin films. The detailed description and operational details of the nebulized spray were reported previously by our research group[11]. In a typical synthesis procedure, 0.1 M of cobalt nitrate hexahydrate ($Co(NO_3)_2.6H_2O$) was

dissolved in 35 ml of double distilled water. The solution was stirred vigorously for 30 min and then appropriate proportion (0, 4, 6 and 8 at.%) of manganese acetate tetrahydrate ($Mn(CH_3COO)_2.4H_2O$) was added as dopant precursor. The mixture was continuously stirred until the precursor components were completely dissolved in the solvent. The obtained solution was filtered using Whatman filter paper to remove the unwanted residual byproducts. The resultant solution was sprayed onto the preheated microscopic glass slides (Blue star, Polar Industrial Corp., India) with coating area of 2.5 × 2.5 cm^2 at a constant temperature of 400 ºC. The spray coating was carried out with a deposition time of 50 s and followed by 2 min break which was repeated for 8 times to complete the whole process. This intermittent spray interval is very helpful in maintaining the substrate temperature and provides sufficient time for nucleation and growth of films. The carrier gas pressure (1.1 kg/cm^2) and nozzle to substrate distance (5 cm) were optimized and kept constant. The whole apparatus was placed in fume hood chamber and the hazardous fumes evolved during deposition were expelled by exhaust system attached to the chamber. Initially, the glass substrates were boiled in chromic acid as a chemical treatment which was followed by cleaning in the soap solution and finally ultrasonicated in acetone and distilled water for 15 min for better adhesion between glass and the deposited film. FTO coated glass substrates (R_{sh} = 15 Ω/sq, Pilkington) purchased from sigma aldrich used only for electrochromic applications were gently cleaned with acetone and allowed to dry in air. The working area of pristine and Mn-doped Co_3O_4 films coated FTO substrates was 1.25 cm^2 with uncoated area of about 0.5 cm^2 utilized for electrical contacts. The obtained films were labeled as MC-0 (pristine Co_3O_4), MC-1 (Mn 4 at.%), MC-2 (Mn 6 at.%) and MC-3 (Mn 8 at.%), respectively.

2.2 Materials characterization

The X-ray diffraction patterns of the Co_3O_4 and Mn-doped Co_3O_4 films were recorded using PANalytical XPert Pro diffractometer (Philips) equipped with Cu-Kα radiation of 1.5406 Å. The scan range (2θ) for investigation was 15 – 80°. The morphology of the films was determined using scanning electron microscope (VEGA 3 TESCAN) with an accelerating voltage of 20 KV attached with EDS (Bruker) for elemental analysis. The chemical state of the films was examined by X-ray photoelectron spectrometer (Kratos Axis Ultra DLD) using Al-Kα as source radiation. Raman spectra of the films were recorded using Seki technotron Raman spectrometer using Ar^+ ion laser (λ = 514 nm). The optical properties of the films were examined from UV visible spectrophotometer (AnTech UV 7000) in the wavelength range of 350 – 1000 nm. The electrical parameters of the deposited films were evaluated by means of linear four probe arrangement coupled with Keithley 2400 source meter. The electrochromic performance of Co_3O_4/FTO films was analyzed by cyclic voltammetry, chronoamperometry and chroncoulometric studies using electrochemical workstation (CH Instrument & Inc., model: CHI604D). A three electrode cell was constructed with platinum (Pt) as the counter electrode, Ag/AgCl was employed as the reference electrode, and Co_3O_4& Mn-doped Co_3O_4/FTO films served as the working electrode. All of them were immersed in 0.5 M of NaOH electrolyte solution. EIS measurements were carried out in the frequency range of 0.01 – 100 KHz by applying a sinusoidal voltage of 5 mV.

3. Results and discussion

3.1. Structural studies

The X-ray diffraction patterns of Co_3O_4 and Mn-doped Co_3O_4 thin films are shown in Fig.1 (a). The obtained films are in polycrystalline nature with preferential orientation along (311) plane. The additional Bragg reflections obtained at 2θ = 18.8º, 31.2º, 44.7º, 59.3º and 65.2º could be attributed to (111), (220), (400), (511) and (440) planes which are good in agreement with Co_3O_4 (JCPDS card no 78-1969). No sign of impurity phases related to MnO_2, Mn_3O_4, and MnCo was observed that indicates that manganese (Mn) ions have been successfully substituted in Co_3O_4. The structural parameters were used to understand the crystallographic properties of the prepared films and the obtained values are listed in Table 1. The crystallite size values of Co_3O_4 and Mn-doped Co_3O_4 thin films were estimated using Scherrer's formula [12] $D = 0.9\lambda/\beta\cos\theta$, where 'β' is the full width at half maximum FWHM, 'λ' is the wavelength of radiation, 'θ' denotes the diffraction angle.

Fig.1 (b) depicts the variation of FWHM and crystallite size of Co_3O_4 films as a function of Mn dopant concentration. In general, the substitution of Mn atom in Co_3O_4 lattice develops a lattice distortion and an intrinsic stress leading to the growth of smaller grains upto 8 at. % of Mn concentration [13]. However, further increase in dopant concentration, the crystallite size value decreases which could be attributed to the saturation limit of manganese substitution in Co_3O_4. A similar type of observation was made by Shalini et al. for Co-doped ZnO thin films by spray pyrolysis [14].

The lattice parameter (a) and microstrain (ε) of Co_3O_4 and Mn-doped Co_3O_4 films were estimated using the following relations [15]:

$$d = \frac{a}{\sqrt{h^2 + k^2 + l^2}} \quad (1)$$

$$\varepsilon = \frac{\beta \cos\theta}{4} \quad (2)$$

where 'd' is the interplanar spacing, 'h', 'k' and 'l' refers to the miller indices. The peak shift towards higher diffraction angles due to the difference in ionic radii of Mn^{2+} (0.67 Å) and Mn^{3+} (0.58 Å) compared to Co^{2+} (0.65 Å) and Co^{3+} (0.61 Å). The presence of two different oxidation states of Mn was confirmed from XPS studies in section 3.3. The substitution of Mn^{3+} ions at Co sites causes reduction in bond length results in unit cell contraction (Table 1) and thereby increases the strain of the deposited films. Pavan kumar et al. has observed similar type of peak shift towards higher diffraction angles and unit cell shrinkage for spray deposited Mn doped CeO_2 films [16].

3.2. Morphological studies

The morphological arrangement of the prepared films was analyzed using scanning electron microscopy and is presented in Fig. 2. From SEM micrographs it is shown that the amount of Mn dopant species has a decisive role in the morphology. Pristine Co_3O_4 (MC-0) exhibited an agglomerated grains, whereas, thin films of Mn-doped Co_3O_4 (MC-1 and MC-2) prepared using 4 and 6 at.% displayed dendrite shaped structures. Few reports are available for the observation of dendrite structures using spray pyrolysis. Afify et al. reported substrate temperature dependence on indium-doped tin oxide films and observed dendrite structures at 525 ºC [17]. Cheng et al. have observed dendrite formation of $LiCoO_2$ films at the substrate temperatures of 400 ºC and 450 ºC fabricated using electrostatic spray deposition route [18]. The

mechanism behind the growth of dendrite pattern in spray pyrolysis is still unknown; Karuppasamy has observed dendrite structure in WO_3 films prepared by co-sputtering method upon Ti doping [19]. Hence, the amount of Mn dopant species may take part in the crystallization process and has driven the self-assembling by coordinating with cobalt and oxygen which leads to the appearance of dendrite structures.

Further increase in Mn dopant concentration to 8 at.% the destruction of dendrites could be correlated to the interstitial occupation of excess Mn atoms affecting the nucleation process. The inset micrograph of MC-2 (higher magnification image) indicates that dendrite pattern was not localized in a particular portion but homogeneously distributed throughout the film surface. Dendrite-like microstructures are more favorable for electrocatalytic applications as they provides enormous channels/pathways for electrolytic ions to diffuse through the film [20].

3.3 Composition analysis

Fig. 3 shows the elemental dispersive X-ray analysis of pure and 6 at.% Mn-doped Co_3O_4 films. The composition quality of the films is realized from the spectra. From the data (inset table), it is observed that the obtained films are near stochiometric in nature. In MC-2 sample a strong Mn peak is located around 5.9 eV which provides an evidence of Mn dopant being successfully substituted in Co_3O_4. The presence of silicon in the spectra arises due to the glass substrate. The atomic percentage (at.%) of Mn is estimated to be 4.93 which is in good agreement of 6 at.% of Mn added in the precursor solution.

Fig. 4 (a) shows the wide scan spectra of nebulizer spray deposited pristine and MC-2 films. From the wide scan spectra it could be notice only the presence of Co, O, Mn and no other

impurities were present except carbon which is due to the sample holder. No signals correspond to any other impurities were detected which indicates the phase purity of the prepared films. To further examine the chemical state of the elements present in the films core level spectra of Co, O and Mn were recorded and displayed in Fig. 4 (b) - (e). The core level O1s spectra shown in Fig. 4 (b) consisting of two well defined peaks: (i) peak located at 529.8 eV correspond to metal-oxygen bonding and (ii) another peak observed at 531.2 eV could be related to surface hydroxyl groups adsorbed over the surface of the film. High resolution spectra of Mn2p contain two broad peaks which were deconvoluted using Gaussian components (Fig. 4 (c)). The spin orbit doublet separation was estimated to be 11.5 eV which is consistent with the previous literatures [16, 21].

It is also ascertained from the deconvoluted spectra that coexistence of both Mn^{2+} and Mn^{3+} ions in MC-2 film from prominent peaks observed at 640.71 and 652.19 eV along with the satellite features obtained at 642.38 and 654.05 eV. The present observation is in good agreement with the reported data in literature [11, 22]. The ionic radius of Mn^{2+} is 0.67 Å which is comparable to ionic radius of Co^{2+} (0.65 Å) and similarly the ionic radius of Mn^{3+} (0.58 Å) is also lesser than the ionic radius of Co^{3+} (0.61 Å) which indicates that the substitution is possible. According to theory of crystal chemistry in spinel type Mn substituted Co_3O_4 (AB_2O_4), the crystal stabilization energy of divalent Co is higher at the octahedral sites (A sites) whereas the trivalent manganese has higher crystal stabilization energy at tetrahedral (B) sites. Hence the occupation of trivalent Mn cations at Co sites results in local lattice distortion due to Jahn-Teller effect [23]. This phenomenon is responsible for the peak shift towards higher diffraction angles and unit cell contraction observed from XRD studies and as well as shift of vibrational modes observed from Raman data. Moreover it has been established that the electrocatalytic property of

spinel Co_3O_4 depends on the ions at the octahedral and tetrahedral sites by the involvement of d-orbitals towards oxygen reduction or evolution reactions [24]. Therefore it can be concluded that occupation of Mn^{2+} and Mn^{3+} ions in Co_3O_4 will be able to control its electrocatalytic activity. The core level spectra Co2p for pristine and MC-2 film shown in Fig. 4 (d) and (e) deconvoluted into Co^{3+} and Co^{2+} ions and it could be observed that peak intensity of Co^{3+} is reduced to a little extent for MC-2 film upon Mn doping. The spin orbit splitting energy value estimated from the Co2p spectra are found to be 15.1 and 15.2 eV for high spin Co^{2+} and low spin Co^{3+} ions respectively [25]. The presence of shakeup satellite features near the prominent peaks also confirms the presence of both Co (II,III) oxidation states in Co_3O_4. A marginal peak shift of about 0.2 eV observed in the case of MC-2 film and Co^{3+} peak reduction could be due to presence of Mn substitution in Co_3O_4.

3.4 Optical studies

Fig. 5 **(**a) shows the optical transmittance of pristine and Mn-doped Co_3O_4 films. The average transmittance values decrease with increase in Mn dopant concentration. This could be attributed to increasing the scattering centers or defects created upon manganese addition. The optical energy band gap (E_g) values of the deposited films were determined from the established Tauc relation [26]:

$$(\alpha h\upsilon)^n = A(h\upsilon - E_g) \qquad (3)$$

where 'α' is the absorption coefficient (cm^{-1}), 'A' is an energy independent constant, 'h' and 'ν' respectively referring to Planck's constant and the frequency of incident light radiation. A plot of $(\alpha h\nu)^2$ vs hν (n=2 for a direct band gap semiconductor) is given in Fig. 5 (b) and the corresponding tangents extrapolated at α=0 provides the band gap of the prepared films. It could

be inferred that the incorporation of manganese dopant atoms manifests a blue shift. The probable reason for this kind of observed variation could be related to the synergistic effect of quantum confinement due to the reduction in the crystallite size, and also the incorporation of Mn atoms alters the bond length between metallic cations (Mn, Co) and O. Both of the above-mentioned phenomena result in poor interaction between the localized orbitals and less overlapping of energy levels. A similar type of observation was made by Le et al.[21].

The refractive index is one of the key optical parameters and depends on the wavelength of incident electromagnetic radiation. Refractive index provides an insight view into electronic polarizability of the ions and local electric field present in the material medium. When an electromagnetic wave passes through a material especially in thin film form, various factors retard its motion and in specific the attenuation and losses due to phonons, absorption of free carriers, generation of secondary photons and scattering [27]. Hence the refractive index of a thin film becomes complex and is a combination of refractive index (n) and extinction coefficient (k) and is denoted by n*. The obtained transmission data are used to deduce the refractive index by employing Swanepoel envelope method [28]:

$$n = [H + (H^2 - S^2)^{\frac{1}{2}}]^{\frac{1}{2}} \quad (4)$$

$$H = \frac{4s^2}{(s^2+1)T^2} - \frac{s^2+1}{2} \quad (5)$$

where ‘s’ is the refractive index of the substrate and it normally taken as ‘1.5’ for glass, ‘H’ is the Swanepoel’s coefficient, ‘T’ refers to the interference-free transmittance generated using an envelope. The extinction coefficient (k) was calculated using the relation: $k = \alpha\lambda/4\pi$. Fig. 6 (a) & (b) shows the variation of refractive index and extinction coefficient with the incident

wavelength of light radiation for pristine and Mn-doped Co_3O_4 thin films. The plots indicate that the refractive index shows anomalous dispersion at lower wavelength region and exhibits normal dispersion at higher wavelengths. Moreover, the extinction coefficient values at the visible region of MC-1 and MC-3 film are higher compared to the values of MC-2 which insist that MC-2 is more favorable for the electrochromic application. The higher extinction coefficient values could be attributed to the rough surface of the MC-1 and MC-3 films increasing the light scattering through the reflection, and in turn, affecting the optical modulation [29]. The obtained results are in line with morphological studies.

The thickness of the deposited films (d) was estimated using the refractive index of adjacent maxima and minima n_1 and n_2 at different wavelengths of λ_1 and λ_2 which is given by the relation [27]:

$$d = \frac{\lambda_1 \lambda_2}{2[\lambda_1 n_2 - \lambda_2 n_1]}. \qquad (6)$$

The obtained thickness values are 685, 730, 785 and 842 nm for pristine (MC-0) and Mn doped Co_3O_4 (MC-1, MC-2, and MC-3) films respectively.

The packing density (P) of the films was evaluated from their refractive index using the method developed by Bragg and Pippard [30] and which was modified later by Macleod [31]:

$$n^2 = \left[\frac{(1-P)n_v^4 + (1+P)n_v n_s^2}{(1+P)n_v^2 + (1-P)n_s^2} \right] \qquad (7)$$

where 'n' is the refractive index of the film at 550 nm and 'n_v' denotes the void refractive index (which is equal to '1' for air). 'n_s' refers to the refractive index of the substrate material.

The estimated packing density values of pristine (MC-0) and Mn-doped Co_3O_4 thin films (MC-1, MC-2 and MC-3) are 2.223, 2.301, 2.177 and 2.251. The change in packing density values might be due to the variation in refractive index with Mn doping content. The packing density values increase initially for the MC-1 film as a result of dense and variation in thickness film due to the addition of Mn content and for the MC-2 film this thickness variation is counterbalanced by porous dendrite morphology as observed from SEM analysis.

Optical dielectric constant (ε_r) is more important in designing an optoelectronic material as it is a complex function. The real part of the dielectric constant (ε_1) corresponding to slowing down the speed of light in a material, and imaginary part (ε_2) contributes to the amount of light energy being absorbed in the electric field of a material due to the dipole moment of atoms [32]. The optical dielectric function is given by:

$$\left.\begin{aligned} \varepsilon_r &= \varepsilon_1 + i\varepsilon_2 \\ \varepsilon_1 &= n^2 - k^2 \\ \varepsilon_2 &= 2nk \end{aligned}\right\} . \qquad (8)$$

Fig. 6 (c) and (d) show the real and imaginary parts of optical dielectric constant dependency on incident wavelength of light radiation. The real part does not show significant variation, whereas, the imaginary part of optical dielectric constant increases with Mn dopant concentration which is consistent with transmission studies.

The lattice dielectric constant (ε_L) and the ratio of free carrier to effective carrier mass (N/m*) can be determined by the following relation [33]:

$$\varepsilon = n^2 = \varepsilon_L - \left(\frac{e^2}{4\pi\varepsilon_0 c^2}\right)\left(\frac{N}{m^*}\right)\lambda^2 \quad (9)$$

where 'e' is the electronic charge (1.6×10^{-19} C), 'c' denotes the velocity of light ($\sim 3 \times 10^8$ m/s), 'ε_0' is the dielectric constant of free space (8.854×10^{-12} F/m). The dependence of n^2 vs. λ^2 as a function of Mn dopant concentration is displayed in Fig. 7 (a).

The intercept and slope values extracted from the curves provides the respective lattice dielectric constant (ε_L) and N/m*. The obtained values are shown in Table 2. The lattice dielectric constant is directly proportional to the phonon vibrations present in the crystal. Mn incorporation in Co_3O_4 has certainly increased the lattice dielectric constant values and the optimum concentration is 6 at.% of Mn (MC-2 film) which has the lowest lattice dielectric constant with high free carrier density. The plasma frequency (ω_p) was formulated by Drude [34] to study the collision between electrons and photons which is given by the following relation:

$$\omega_p = \left(\frac{e^2(N/m^*)}{\varepsilon_0}\right)^{1/2} \quad (10)$$

The plasma frequency values (Table 2) increase with doping concentration as a consequence of the increase in carrier density according to Drude free electron theory [35].

Wemple – DiDomenico proposed a single oscillator model which has the ability to fit the dispersive refractive index as a function of photon energy (hν) for most of the semiconducting materials [36]:

$$n^2 = 1 + \frac{E_0 E_d}{{E_0}^2 - (h\nu)^2} \quad (11)$$

where 'E_d' refers to dispersion energy or the oscillator strength which is associated with the interband transitions, 'E_0' is effective oscillator energy. A plot of n^2 vs hv (eV) for pristine and Mn-doped Co_3O_4 films is given in Fig. 7 (b). The intercept $(E_0E_d)^{-1}$ and slope $(E_0/E_d)^{-1}$ of linear fitted curve provides single oscillator parameters E_0 and E_d and they are listed in Table 2.

The dispersion energy 'E_d' value decreases with Mn dopant concentration related to the distortion and strain caused by Mn occupation in Co_3O_4 lattice sites modifying the interband optical transitions between $Co^{2+} \leftrightarrow Co^{3+}$ in the energy band structure. A similar type of observation was made by Boukhachem et al. for sprayed Co-doped MoO_3 films [37]. The effective oscillator energy 'E_0' could be directly proportional to optical band gap which follows an empirical relation $E_0 \approx 2.0\ E_g$ established by Tanaka et al. [38]. The obtained values are in close agreement with the empirical relation. The static refractive index (zero frequency refractive index) values of the deposited films were estimated from the following equation:

$$n_0 = \sqrt{\left(1 + \frac{E_d}{E_0}\right)} \quad . \tag{12}$$

The static refractive index values show a fractional decrement with Mn dopant concentration. The observed values given in Table 2 are in good agreement with Cd-doped copper ferrite films [39].

3.5. Raman spectroscopy

Raman spectroscopy provides useful and detailed structural information such as phase identification, the formation of phase transitions on doping/alloying, the strength of chemical bonding between atoms and it is highly receptive to the local environment of cations in semiconducting metal oxides. Fig. 8 shows the Raman spectra of Co_3O_4 and Mn-doped Co_3O_4

thin films. From the figure, the peaks located at 194, 480, 522, 620 and 690 cm^{-1} correspond to F_{2g} (1), E_g, F_{2g} (2), F_{2g} (3) and A_{1g} vibrational modes respectively [40]. The most intense peak at high-frequency mode 690 cm^{-1} is considered as the characteristic peak of spinel type cobalt oxides [3]. Two significant observations were made from the spectra: (i) increment in peak intensity of F_{2g} (1) and (ii) the shift of low and high-frequency modes obtained at 194 cm^{-1} and 690 cm^{-1} upon increase in Mn doping concentration. This inference indicates incorporation of Mn dopant equally at both octahedral and tetrahedral sites of Co_3O_4, because of the low and high frequency modes related to stretching vibration of tetrahedral sites and symmetric vibration at octahedral sites. A similar type of observation was made by Giovannelli et al. for $(Co_{1-x}Mn_x)_3O_4$ nanoparticles [41]. There are no peaks observed related to the existence of other impurity phases of Co or Mn and mixed oxides which shows phase purity of the prepared films and it is consistent with X-ray diffraction studies. The broadening of A_{1g} vibrational mode could be attributed to either increase in lattice vibrations or formation of structural disorder owing to Mn addition [41].

3.6. Electrical studies

The electrical properties of the films were studied using linear four probe arrangement. The electrical parameters such as sheet resistance, resistivity, and activation energy were listed in Table 3. From Table 3 it can be observed that resistivity of Co_3O_4 films (MC-1 & MC-2) decreases with increase in Mn dopant concentration upto 6 at.%. Co_3O_4 compared to pristine Co_3O_4 film (MC-0). The partial occupation of mixed valance states $Mn^{2+}(3d^4)$ and $Mn^{3+}(3d^3)$ at the lattice sites of $Co^{2+}(3d^7)$ and $Co^{3+}(3d^6)$ in the complex spinel structured cubic Co_3O_4 eventually boosts the hole concentration and thereby enhances the electrical conductivity.

The low sheet resistance of the MC-2 film is more favorable for electrochromic applications since less electrical stimulus is required to exhibit faster and higher response to bleaching and coloration reactions [42]. The decrement in the sheet resistance was presumably due to the reduction in the number of grain boundaries as the peaks other than the predominant plane (311) suppressed to a greater extent upon Mn doping which could be recognized from XRD results. Therefore the Mn substitutional doping effectively increases the charge mobility as the grain boundaries severely restrict the motion of charge carriers. Further increase in Mn concentration to 8 at.% (MC-3) leads to a decline of electrical conductivity as the excess Mn content segregates at grain boundaries which in turn contributes to trapping of charge carriers. The obtained results are in accordance with the literature [43]. Fig. 9 shows the Arrhenius behavior (ln ρ vs 1000/T(K)) of Co_3O_4 and Mn-doped Co_3O_4 films. The entire films prepared using nebulized spray deposition exhibited semiconducting nature as there was a fall in resistivity with the increase in temperature. The activation energy (E_a) of the films was determined by fitting the experimental data linearly using Arrhenius law and is given by [9]:

$$\rho = \rho_0 \exp\left(\frac{E_a}{kT}\right) \tag{13}$$

where 'ρ_0' is the pre-exponential factor, 'K' refers to Boltzmann constant, and 'T' is the temperature. The small deviation observed in the activation energy values (Table 3) is due to the changes in stoichiometry of Co_3O_4 as a consequence of Mn incorporation [44].

3.7. Electrochromic studies:

Cyclic voltammetry (CV) curves of pristine and Mn-doped Co_3O_4 cycled in 0.5 M of NaOH solution with a scan rate of 50 mV/s are given in Fig. 10 (a). A single redox couple was observed during the scan process and the obtained cyclic voltammograms are in good agreement with

earlier reports [45, 46]. The reactions involved in the coloration and bleaching process of Co_3O_4/FTO electrodes are:

Anodic scan (Positive potential):

$$3Co(OH)_2 + 2\ OH^- \rightarrow Co_3O_4 + 4H_2O + e^- \qquad (14)$$

Cathodic scan (Negative Potential):

$$Co_3O_4 + H_2O + 2e^- \rightarrow 3Co(OH)_2 + 2\ OH^- . \qquad (15)$$

Some of the interesting observations were made in cyclic voltammetric studies of the deposited films due to the addition of dopant Mn in Co_3O_4. The cathodic and anodic peak current density values amplified dramatically with Mn dopant concentration which could be correlated with low resistivity and high electrical conductivity observed from electrical studies and also the decrease in the contact resistance between Co_3O_4 and FTO as evident from EIS studies (Fig. 10 (d)). The potential window used for CV scan is swept from -1.2 to +1.1 V for pristine Co_3O_4 and -0.6 to +0.8 V for Mn-doped Co_3O_4 films. Gobal and Jafarzadeh [47] have inferred the similar type of variation for manganese deposited over cobalt oxide layers where the enhancement in the current density of the anodic and cathodic peaks at the cost of the reduction in the potential window was observed. Similar type of observation was also made by Naveen and Selladurai [4]. The possible reason for this unusual behavior could be due to promotion of ionic conductivity of Co_3O_4 film upon Mn doping. It is worth to mentioning that no addition peaks were observed corresponding to manganese even at higher dopant concentration, which signifies that manganese, does not have any contribution to the electrochemical activity.

The diffusion coefficient values of the films were derived using the Randles-Sevcik relation which is given by [48]:

$$D^{1/2} = \frac{J_p}{2.72\times10^5 \times n^{3/2} \times C_0 \times v^{1/2}} \quad (16)$$

where 'J_p' denotes the anodic or cathodic peak current density (mA/cm^2), C_0 is the concentration of the electrolytic ions (mol/cm^3), n is the number of electrons participated in the reaction (which is normally equal to '1'), and 'ν' refers to the scan rate (mV/s). The diffusion coefficient values and other electrochemical parameters acquired from CV studies were summarized in Table 4. The obtained diffusion coefficient values are higher than Li^+ ion diffusion in V_2O_5-WO_3 films (order of 10^{-18} cm^2/s) prepared by pulsed chemical spray pyrolysis [49] and comparable to spin-coated Co-doped NiO thin films (10^{-13} cm^2/s) in KOH electrolyte [50].

The film MC-2 has shown higher diffusion coefficient values among other deposited films and notably it has a large integral CV curve area with minimum potential separation indicating better reversibility. The crystallite size and dendrite morphology play a key role in determining the transfer rate of ionic diffusion species. Nanocrystalline nature with dendrite morphology of MC-2 film provides the high surface-to-volume ratio as the porous structure allows facile diffusion of ions and moreover, Mn doping also creates more pathways for ion insertion/extraction. Even though MC-1 exhibited dendrite pattern the porosity of the film is low which appears to be cluster and denser compared to MC-2. The diffusion mechanism behind the cluster and porous dendrite-shaped structures is presented schematically in Fig. 11.

The amount of charges inserted and extracted during the electrochromic intercalation and deintercalation process was evaluated by chronocoulometry for pristine and Mn-doped Co_3O_4 films which were measured at a potential of ± 0.8 V with duration of 10 s for each step (coloration/bleaching) and the obtained graphs are shown in Fig. 10(b). The reversibility (%) of

the films is defined as the ratio of the quantity of charge extracted (Q_{di}) to the charge inserted (Q_i) during the reaction. The electrochemical parameters obtained from chronocoulometry curves are given in Table 5. The maximum reversibility value observed for MC-2 film attributed to its better morphology and which creates additional channels for ion insertion/extraction upon Mn doping.

Potential step chronoamperometric experiments were conducted to analyze the switching kinetics for pristine and Mn-doped Co_3O_4 films for the step of 10 s between -0.8 to +0.8 V vs. Ag/AgCl and the obtained profiles are presented in Fig. 10(c). The amount of time required to complete one coloration and bleaching cycle could be determined from current – time transient graph and is denoted as t_b (time for bleaching) and t_c (time for coloring). The obtained bleaching and coloration switching values are listed in Table 6. The switching time of MC-1 increases marginally compared to pristine Co_3O_4 owing to its dense nature as a result of an increase in thickness with Mn concentration and it is compensated by increased porous nature with low crystallite size observed for the MC-2 film [51]. The poor switching kinetics of MC-3 film possibly is due to excess Mn content which acts as an impurity segregated at the grain boundaries block the easy flow of OH^- ions.

To gain more insight into diffusion kinetics and charge transport phenomena of the prepared films EIS measurements were made and the obtained Nyquist plots are displayed in Fig. 10 (d) and the corresponding equivalent circuit shown in Fig. 10 (e) which is used to fit the impedance data. The impedance spectra consisted of three regions: (i) the initial or the beginning point of the curve near to the origin refers to series resistance (R_s) which is the sum of contact resistance between Co_3O_4/FTO, electrolyte resistance and resistance of FTO electrode, (ii) The

second part of the impedance curve i.e., the diameter of the semicircle arc corresponds to charge transfer resistance (R_{ct}). The component 'C_{dl}' present in the equivalent circuit is related with double layer capacitance also called as constant phase angle element (CPE). The series resistance values are found to be 18.72, 14.45, 12.27 and 19.6 $\Omega.cm^2$ for MC-0, MC-1, MC-2 and MC-3 films, respectively. The low series resistance values of MC-2 could be attributed to high conductivity observed from electrical measurements. The obtained charge transfer resistance values are 3.88, 1.71, 1.55 and 6.31 $\Omega.cm^2$ for MC-0, MC-1, MC-2 and MC-3 films, respectively. The inclined linear line after the semicircular arc denotes the Warburg impedance (Z_W) related to the ion diffusion process. Normally if the angle of inclination is greater than 45° it ensures more accessibility of OH^- ions at the electrode surface [52]. Therefore, we believe that MC-2 film (Mn 6 at.%) with low R_s and R_{ct} is more suitable for electrochromic applications.

The optical properties of the colored and bleached states of pristine and Mn-doped Co_3O_4 films were determined from UV-Visible transmission spectra shown in Fig. 12. The parameters such as transmittance modulation (ΔT), optical density (ΔOD) and photopic contrast ratio (PCR) of the bleached and colored states at a particular incident wavelength (λ=633 nm) were estimated from the following relations [53]:

$$\Delta T = T_b - T_c; \quad \text{PCR} = \left[\frac{T_b}{T_c}\right] \text{ and } \Delta\text{OD} = \ln\left(\frac{T_b}{T_c}\right) \qquad (17)$$

The coloration efficiency (CE) is the figure of merit to understand the optical modulation that happens after charge insertion/extraction. It is defined as the ratio of optical density to the total amount of charges intercalated (Q_{in}) per unit electrode area which is given by:

$$CE = \frac{\Delta OD(\lambda)}{Q_{in}} \tag{18}$$

The obtained values of optical modulation parameters are presented in Table 6. The maximum CE efficiency (29.6 cm^2/C) obtained for MC-2 film is comparable to cobalt oxide nanowalls (31 cm^2/C) synthesized by CBD and porous Co_3O_4 (30 cm^2/C) fabricated by self-assembled template techniques [3, 54], but it is higher than Co_3O_4 films prepared by CVD (21.5 cm^2/C) and electro-deposition methods (20.5 cm^2/C) [54, 55]. Till now, the maximum CE of 42 cm^2/C has been achieved by Zhang et al. for hexamethyl tetra amine assisted porous Co_3O_4 nanowall arrays synthesized by CBD method [3], which is slightly higher than the CE obtained in our present work. Similarly the transmittance modulation value of MC-2 film in the visible range (35 %) is higher among the prepared films and other methods such as sol-gel and sputtering (15 %) [56, 57], but, it is comparable to random porous Co_3O_4 films (40 %) prepared by electrodeposition and chemical bath deposition [54, 58].

The positive recognition observed from MC-2 film could be attributed to the following factors: (i) nanocrystalline nature of Mn doped Co_3O_4 as inferred from XRD results, (ii) porous dendrite microstructures with high electrical conductivity, (iii) high diffusion coefficient values obtained from CV results and (iv) low charge transfer resistance observed from Nyquist plots. The above mentioned-factors are responsible for shortening of ion diffusion path length and thereby enhancing the electrochromic performance, optical modulation, and coloration efficiency. It is important to notice that manganese (Mn) is more cost-effective compared to cobalt (Co) and hence a small portion of Co is replaced by Mn could provide efficient electrochromic devices at low cost. The observed coloration efficiency of the film may be improved further by modifying the spray deposition conditions for electrochromic applications.

4. Conclusions

Pristine and Mn-doped Co_3O_4 films were successfully deposited using nebulizer spray technique for different dopant concentrations (4, 6 and 8 at.%). X-ray diffraction patterns revealed that the obtained films crystallized in cubic spinel structure with predominant orientation along (311) plane and reduction in crystallite size were observed with increase in Mn dopant concentration. The growth of dendrites may be due to the self-assembly process upon Mn incorporation. The optical dispersion parameters and low electrical resistivity suggested that the optimum condition of Mn doping (6 at.%) is more suitable for electrochromic applications and also porous dendrite morphology of MC-2 film supports enhancement of optical parameters. The maximum coloration efficiency of 29 cm^2/C with high optical contrast of 35% was observed for 6 at.% (MC-2) of Mn-doped porous dendrite-shaped Co_3O_4 film.

References

[1] C.G. Granqvist, Handbook of Inorganic Electrochromic Materials, Elsevier Science, 1995.
[2] C.G. Granqvist, Thin Solid Films, 564 (2014) 1-38.
[3] C. Zhang, C. Zheng, S. Zhou, Y. Shen, C. Zuo, Mater. Res. Bull., 89 (2017) 204-209.
[4] A.N. Naveen, S. Selladurai, Electrochim. Acta, 125 (2014) 404-414.
[5] R. Jin, Y. Meng, Y. Ma, H. Li, Y. Sun, G. Chen, Electrochim. Acta, 209 (2016) 163-170.
[6] Y. Zhang, S. Liu, Y. Li, D. Deng, X. Si, Y. Ding, H. He, L. Luo, Z. Wang, Biosens. Bioelectron., 66 (2015) 308-315.
[7] X. Cao, W. Yan, C. Jin, J. Tian, K. Ke, R. Yang, Electrochim. Acta, 180 (2015) 788-794.
[8] K. Punitha, R. Sivakumar, C. Sanjeeviraja, J. Appl. Phys., 115 (2014) 113512.
[9] C.R. Dhas, R. Venkatesh, R. Sivakumar, A.M.E. Raj, C. Sanjeeviraja, Opt. Mater., 72 (2017) 717-729.
[10] S.S. Latthe, P. Sudhagar, C. Ravidhas, A. Jennifer Christy, D. David Kirubakaran, R. Venkatesh, A. Devadoss, C. Terashima, K. Nakata, A. Fujishima, CrystEngComm, 17 (2015) 2624-2628.
[11] C. Ravi Dhas, R. Venkatesh, A. Jennifer Christy, D. Arivukarasan, B. Anitha, D. David Kirubakaran, A. Juliat Josephine, P. Sudhagar, A. Moses Ezhil Raj, C. Sanjeeviraja, Recent Trends in Materials Science and Applications, Springer International Publishing, pp. 351-365.
[12] B.D. Cullity, S.R. Stock, Elements of X-Ray Diffraction: Pearson New International Edition, Pearson Education, Limited, 2013.
[13] C. Mrabet, A. Boukhachem, M. Amlouk, T. Manoubi, J. Alloys Compd., 666 (2016) 392-405.
[14] S. Shalini, D. Balamurugan, J. Colloid Interface Sci., 466 (2016) 352-359.
[15] C. Ravi Dhas, R. Venkatesh, D. David Kirubakaran, J. Princy Merlin, B. Subramanian, A. Moses Ezhil Raj, Mater. Chem. Phys., 186 (2017) 561-573.
[16] C.S.S. Pavan Kumar, R. Pandeeswari, B.G. Jeyaprakash, J. Alloys Compd., 602 (2014) 180-186.
[17] H.H. Afify, F.S. Terra, R.S. Momtaz, Journal of Materials Science: Materials in Electronics, 7 (1996) 149-153.
[18] C. Chen, E.M. Kelder, P.J.J.M. van der Put, J. Schoonman, J. Mater. Chem., 6 (1996) 765-771.
[19] A. Karuppasamy, Appl. Surf. Sci., 359 (2015) 841-846.
[20] L. Zhang, X. Zhao, W. Ma, M. Wu, N. Qian, W. Lu, CrystEngComm, 15 (2013) 1389-1396.
[21] T.L. Le, S. Guillemet-Fritsch, P. Dufour, C. Tenailleau, Thin Solid Films, 612 (2016) 14-21.
[22] J.-Y. Wang, P.-Y. Kuang, N. Li, Z.-Q. Liu, Y.-Z. Su, S. Chen, Ceram. Int., 41 (2015) 8670-8679.
[23] J. Li, X. Liang, S. Xu, J. Hao, Applied Catalysis B: Environmental, 90 (2009) 307-312.
[24] E. Lee, J.-H. Jang, Y.-U. Kwon, J. Power Sources, 273 (2015) 735-741.

[25] N. Zhang, Q. Qin, X. Ma, J. Zhou, L. Sun, C. Chen, S. Wen, Y. Chen, S. Ruan, J. Alloys Compd., 723 (2017) 779-786.
[26] C.R. Dhas, R. Venkatesh, R. Sivakumar, A.M.E. Raj, C. Sanjeeviraja, Ionics, 22 (2016) 1911-1926.
[27] J. Singh, Optical Properties of Condensed Matter and Applications, Wiley, 2006.
[28] R. Swanepoel, Journal of Physics E: Scientific Instruments, 16 (1983) 1214.
[29] J.-h. Zhang, G.-f. Cai, D. Zhou, H. Tang, X.-l. Wang, C.-d. Gu, J.-p. Tu, Journal of Materials Chemistry C, 2 (2014) 7013-7021.
[30] W.L. Bragg, A.B. Pippard, Acta Crystallographica, 6 (1953) 865-867.
[31] H.A. Macleod, Journal of Vacuum Science & Technology A: Vacuum, Surfaces, and Films, 4 (1986) 418-422.
[32] S. Sarkar, N.S. Das, K.K. Chattopadhyay, Solid State Sciences, 33 (2014) 58-66.
[33] M. El-Nahass, M. Emam-Ismail, M. El-Hagary, J. Alloys Compd., 646 (2015) 937-945.
[34] C. Kittel, Introduction to Solid State Physics, Wiley, 2004.
[35] M. Kadi, A. Smaali, R. Outemzabet, Surf. Coat. Technol., 211 (2012) 45-49.
[36] S. Wemple, M. DiDomenico Jr, Physical Review B, 3 (1971) 1338.
[37] A. Boukhachem, M. Mokhtari, N. Benameur, A. Ziouche, M. Martínez, P. Petkova, M. Ghamnia, A. Cobo, M. Zergoug, M. Amlouk, Sensors and Actuators A: Physical, 253 (2017) 198-209.
[38] K. Tanaka, Thin Solid Films, 66 (1980) 271-279.
[39] M. El-Hagary, A. Matar, E. Shaaban, M. Emam-Ismail, Mater. Res. Bull., 48 (2013) 2279-2285.
[40] V. Hadjiev, M. Iliev, I. Vergilov, Journal of Physics C: Solid State Physics, 21 (1988) L199.
[41] F. Giovannelli, V. Marsteau, M. Zaghrioui, C. Autret, F. Delorme, Adv. Powder Technol., 28 (2017) 1325-1331.
[42] L. Bertus, A. Enesca, A. Duta, Thin Solid Films, 520 (2012) 4282-4290.
[43] D.R. Acosta, C. Magaña, F. Hernández, J. Ortega, Thin Solid Films, 594 (2015) 207-214.
[44] A. Bagade, V. Ganbavle, S. Mohite, T. Dongale, B. Sinha, K. Rajpure, J. Colloid Interface Sci., 497 (2017) 181-192.
[45] K.K. Purushothaman, B. Sethuraman, M.P. Anupama, M. Dhanasankar, G. Muralidharan, Mater. Sci. Semicond. Process., 16 (2013) 1410-1415.
[46] X.H. Xia, J.P. Tu, J. Zhang, X.H. Huang, X.L. Wang, W.K. Zhang, H. Huang, Electrochem. Commun., 10 (2008) 1815-1818.
[47] F. Gobal, S. Jafarzadeh, J. Solid State Electrochem., 16 (2012) 1561-1569.
[48] A.J. Bard, L.R. Faulkner, J. Leddy, C.G. Zoski, Electrochemical methods: fundamentals and applications, wiley New York, 1980.
[49] C. Patil, N. Tarwal, P. Jadhav, P. Shinde, H. Deshmukh, M. Karanjkar, A. Moholkar, M. Gang, J. Kim, P. Patil, Current Applied Physics, 14 (2014) 389-395.
[50] K. Purushothaman, G. Muralidharan, J. Non-Cryst. Solids, 358 (2012) 354-359.
[51] J. Zhang, J.-p. Tu, X.-h. Xia, X.-l. Wang, C.-d. Gu, J. Mater. Chem., 21 (2011) 5492-5498.

[52] J. Deng, L. Kang, G. Bai, Y. Li, P. Li, X. Liu, Y. Yang, F. Gao, W. Liang, Electrochim. Acta, 132 (2014) 127-135.
[53] T. Dhandayuthapani, R. Sivakumar, R. Ilangovan, C. Gopalakrishnan, C. Sanjeeviraja, A. Sivanantharaja, Electrochim. Acta, 255 (2017) 358-368.
[54] Y.F. Yuan, X.H. Xia, J.B. Wu, J.S. Gui, Y.B. Chen, S.Y. Guo, Journal of Membrane Science, 364 (2010) 298-303.
[55] T. Maruyama, S. Arai, J. Electrochem. Soc., 143 (1996) 1383-1386.
[56] W. Estrada, M. Fantini, S. De Castro, C. Polo da Fonseca, A. Gorenstein, J. Appl. Phys., 74 (1993) 5835-5841.
[57] F. Švegl, B. Orel, M. Hutchins, K. Kalcher, J. Electrochem. Soc., 143 (1996) 1532-1539.
[58] X.H. Xia, J.P. Tu, J. Zhang, X.H. Huang, X.L. Wang, X.B. Zhao, Electrochim. Acta, 55 (2010) 989-994.

Figure Captions:

Fig.1 (a) X-ray diffraction patterns of pristine and Mn-doped Co_3O_4 thin films and (b) dependence of crystallite size and FWHM over Mn dopant concentration.

Fig. 2 SEM micrographs of pristine and Mn-doped Co_3O_4 thin films

Fig. 3 EDX spectra of pristine and 6 at.% of Mn-doped Co_3O_4 films.

Fig. 4: (a) XPS wide survey scan, (b), (c), (d) & (e) core level spectra of O1s, Mn2p and Co2p of pristine and MC-2 films.

Fig. 5 (a) Transmittance spectra and (b) Tauc plot of pristine and Mn-doped Co_3O_4 thin films.

Fig. 6 (a) Refractive index (b) extinction coefficient (c) & (d) optical dielectric constants of Co_3O_4 and Mn-doped Co_3O_4 thin films.

Fig. 7 A plot of (a) λ^2 vs. n^2 and (b) relation between $(n^2-1)^{-1}$ and $(hv)^2$ for Co_3O_4 films as a function of dopant concentration.

Fig. 8 Raman spectra of Co_3O_4 and Mn-doped Co_3O_4 thin films.

Fig. 9 Arrhenius plot of Co_3O_4 and Mn-doped Co_3O_4 films.

Fig. 10 Electrochemical characterization of Co_3O_4 and Mn-doped Co_3O_4 films cycled in 0.5 M NaOH solution, (a) Cyclic voltammetry curves (b) & (c) chronocoulometry and chronoamperometry profiles (d) Nyquist plots, and (e) Equivalent circuit used to fit the data.

Fig. 11 Schematic representation of diffusion pathways in Mn doped Co_3O_4 dendrite structures.

Fig. 12 Transmission spectra of bleached and colored states of pure and Mn-doped Co_3O_4 films.

Table Captions:

Table 1 Crystalline parameters of Co_3O_4 and Mn-doped Co_3O_4 films*

Table 2 Optical parameters of Co_3O_4 and Mn-doped Co_3O_4 films

Table 3 Electrical parameters of Co_3O_4 and Mn-doped Co_3O_4 films

Table 4 Electrochemical parameters of pristine and Mn-doped Co_3O_4 films

Table 5 Q_i, Q_{di} and reversibility of pristine and Mn-doped Co_3O_4 films

Table 6 Switching response, Optical modulation and Coloration efficiency of pristine and Mn-doped Co_3O_4 films

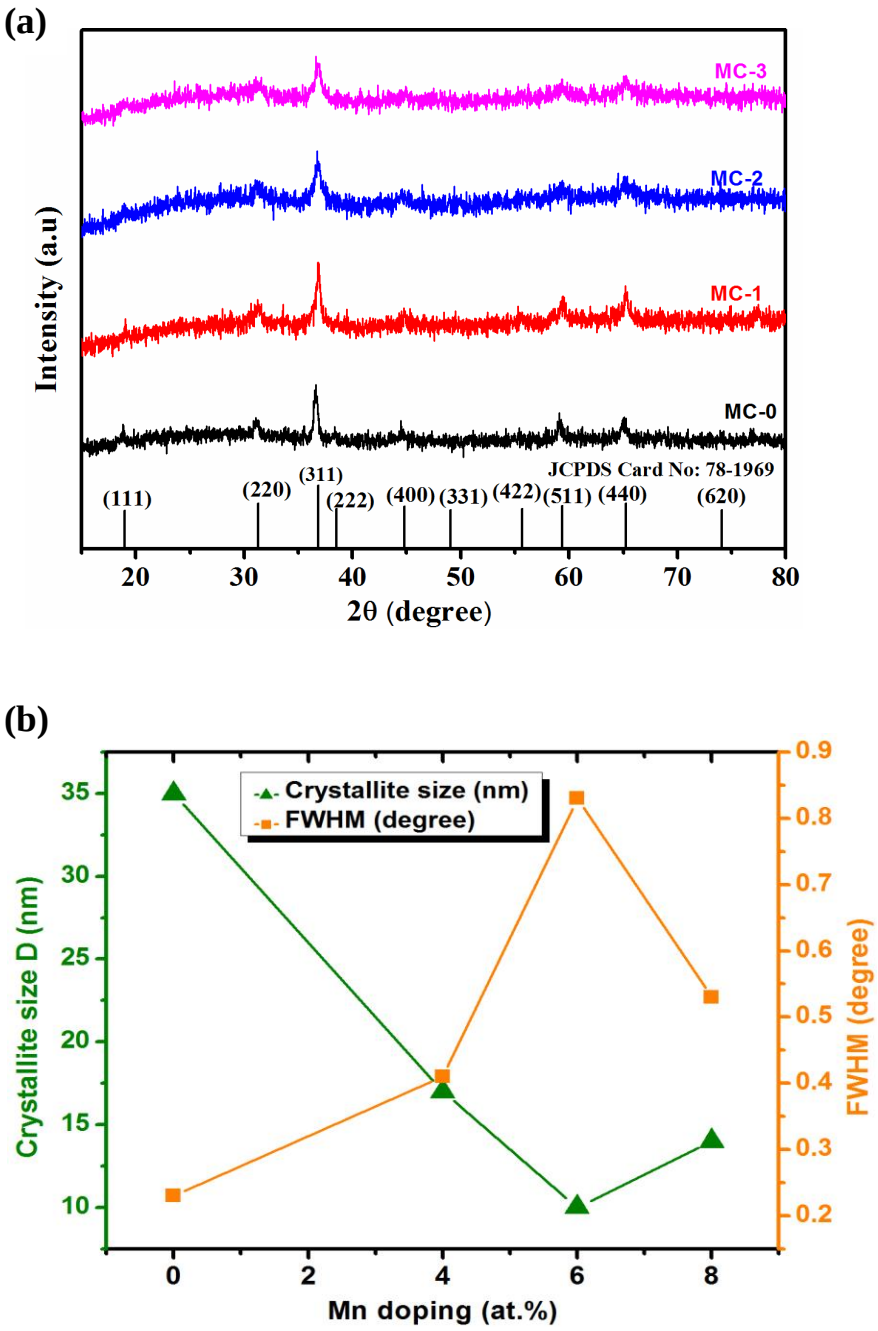
(a)
MC-3
MC-2
MC-1
MC-0
Intensity (a.u)
JCPDS Card No: 78-1969
(111)
(220)
(311)
(222)
(400)
(331)
(422)
(511)
(440)
(620)
20
30
40
50
60
70
80
2θ (degree)
(b)
Crystallite size (nm)
FWHM (degree)
Crystallite size D (nm)
FWHM (degree)
35
30
25
20
15
10
0.9
0.8
0.7
0.6
0.5
0.4
0.3
0.2
0
2
4
6
8
Mn doping (at.%)

Fig.1

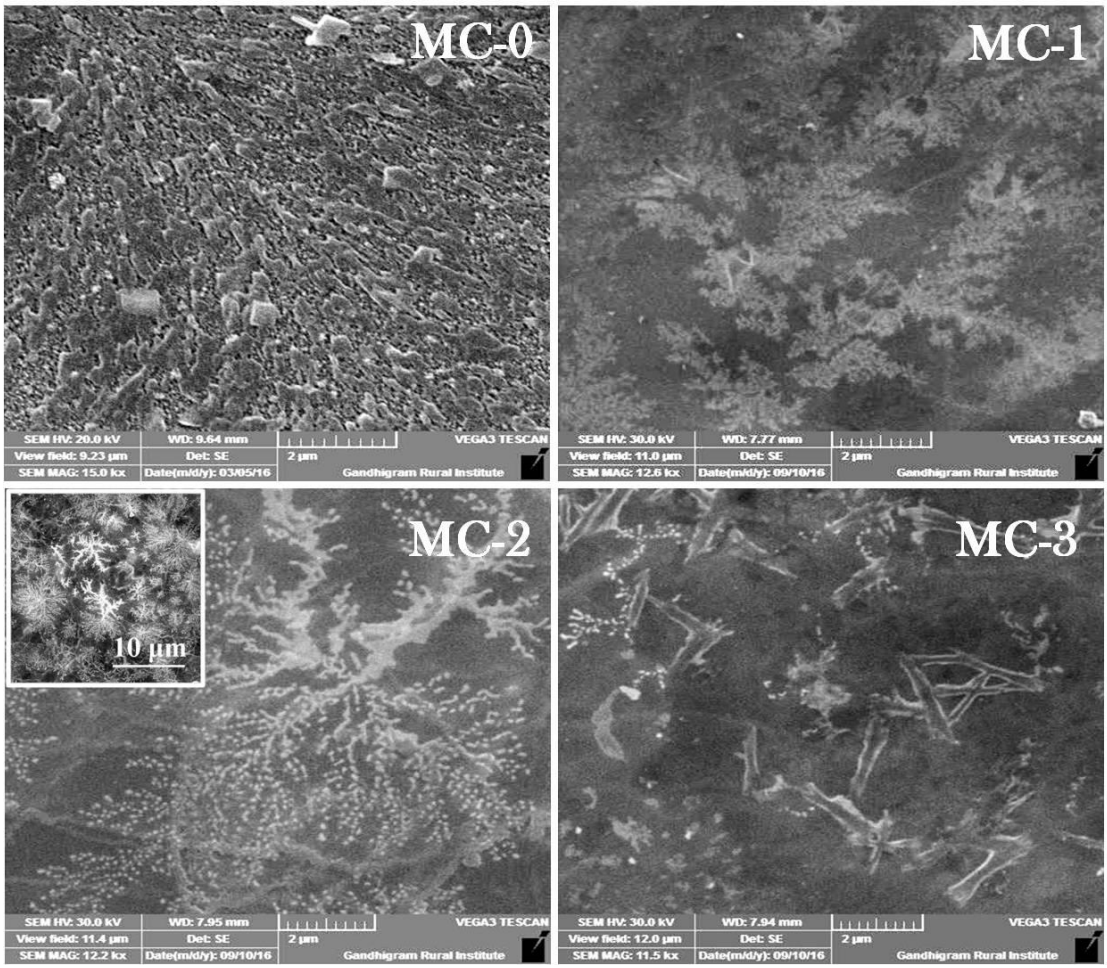
MC-0
SEM HV: 20.0 kV
WD: 9.64 mm
VEGA3 TESCAN
View field: 9.23 µm
Det: SE
2 µm
SEM MAG: 15.0 kx
Date(m/d/y): 03/05/16
Gandhigram Rural Institute
MC-1
SEM HV: 30.0 kV
WD: 7.77 mm
VEGA3 TESCAN
View field: 11.0 µm
Det: SE
2 µm
SEM MAG: 12.6 kx
Date(m/d/y): 09/10/16
Gandhigram Rural Institute
MC-2
10 µm
SEM HV: 30.0 kV
WD: 7.95 mm
VEGA3 TESCAN
View field: 11.4 µm
Det: SE
2 µm
SEM MAG: 12.2 kx
Date(m/d/y): 09/10/16
Gandhigram Rural Institute
MC-3
SEM HV: 30.0 kV
WD: 7.94 mm
VEGA3 TESCAN
View field: 12.0 µm
Det: SE
2 µm
SEM MAG: 11.5 kx
Date(m/d/y): 09/10/16
Gandhigram Rural Institute

Fig. 2

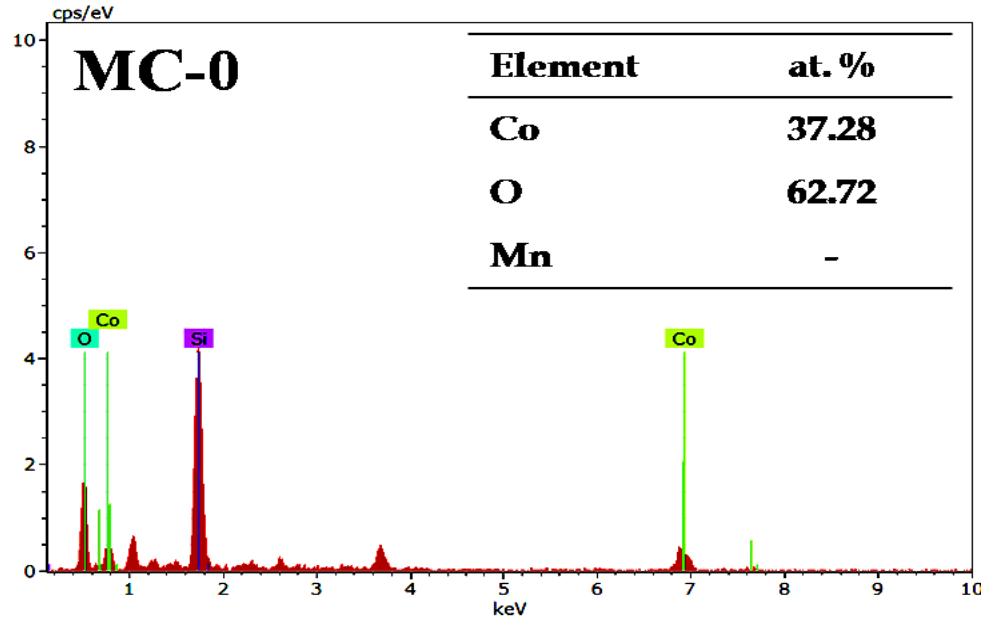
cps/eV
MC-0
Element at. %
Co 37.28
O 62.72
Mn -
Co
O
Si
Co
keV

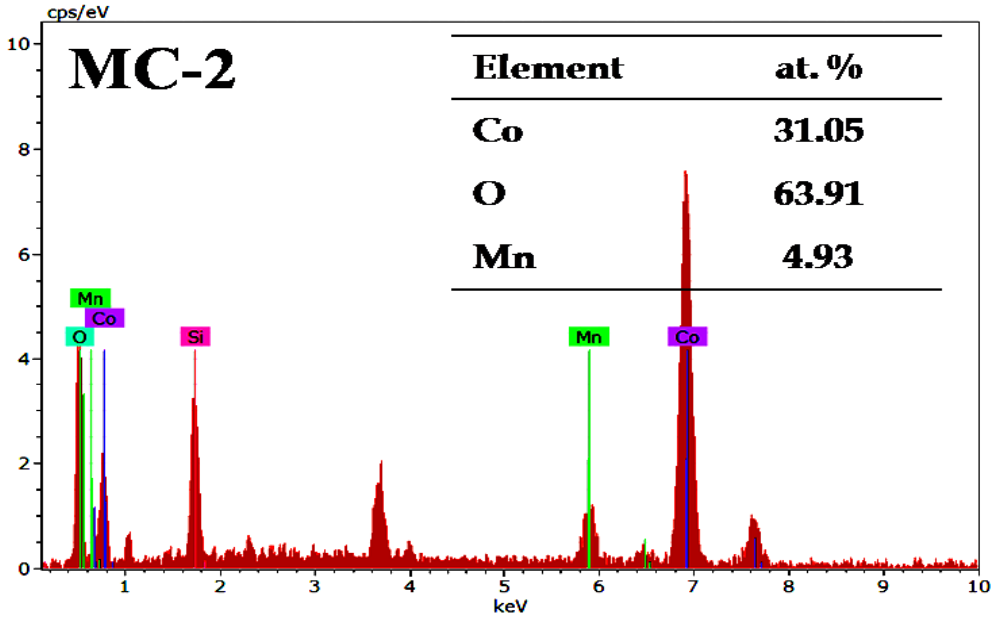
cps/eV
MC-2
Element at. %
Co 31.05
O 63.91
Mn 4.93
Mn
Co
O
Si
Mn
Co
keV

Fig. 3

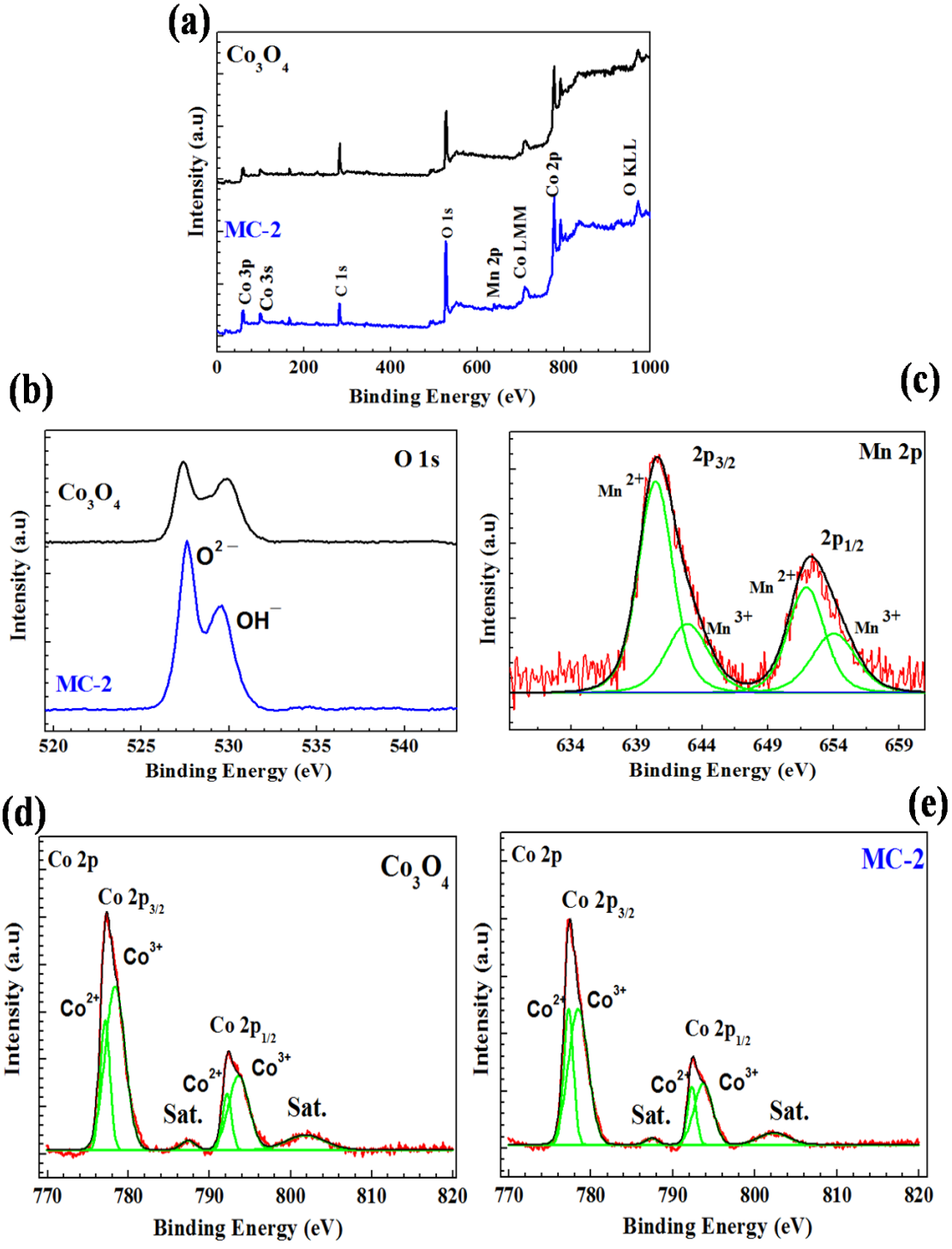
(a)
Co3O4
MC-2
Intensity (a.u)
Co 3p
Co 3s
C 1s
O 1s
Mn 2p
Co LMM
Co 2p
O KLL
0
200
400
600
800
1000
Binding Energy (eV)
(b)
O 1s
Co3O4
O2−
OH−
MC-2
Intensity (a.u)
520
525
530
535
540
Binding Energy (eV)
(c)
Mn 2p
2p3/2
Mn 2+
Mn 3+
2p1/2
Mn 2+
Mn 3+
Intensity (a.u)
634
639
644
649
654
659
Binding Energy (eV)
(d)
Co 2p
Co3O4
Co 2p3/2
Co3+
Co2+
Co 2p1/2
Co2+
Co3+
Sat.
Sat.
Intensity (a.u)
770
780
790
800
810
820
Binding Energy (eV)
(e)
Co 2p
MC-2
Co 2p3/2
Co2+
Co3+
Co 2p1/2
Co2+
Co3+
Sat.
Sat.
Intensity (a.u)
770
780
790
800
810
820
Binding Energy (eV)

Fig. 4

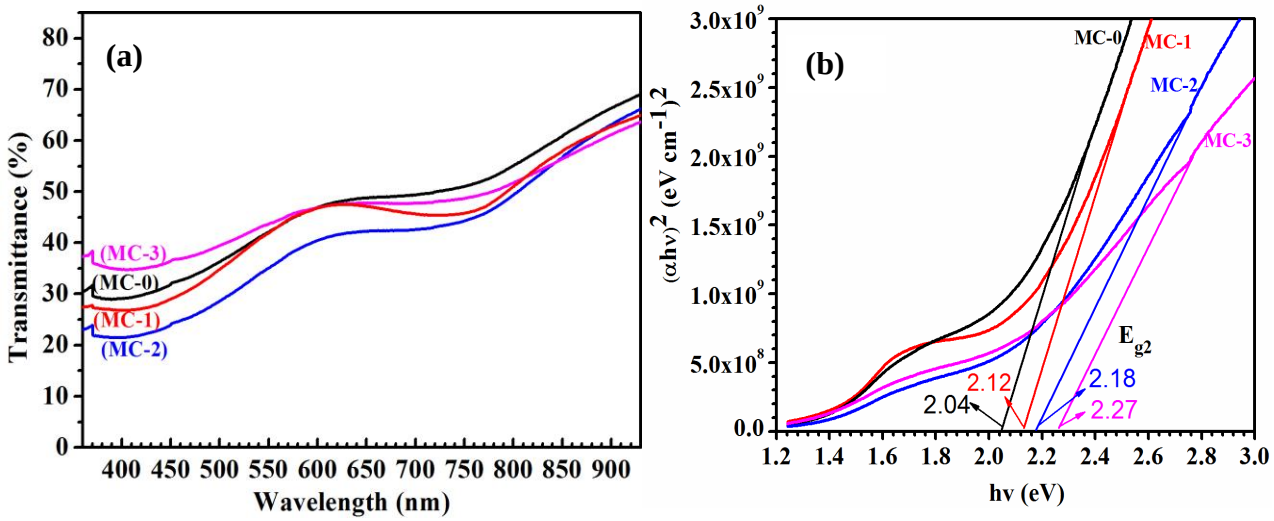
(a)
Transmittance (%)
Wavelength (nm)
(MC-3)
(MC-0)
(MC-1)
(MC-2)
(b)
$(\alpha h\nu)^2$ (eV cm^{-1})2
hv (eV)
MC-0
MC-1
MC-2
MC-3
E_{g2}
2.12
2.04
2.18
2.27

Fig. 5

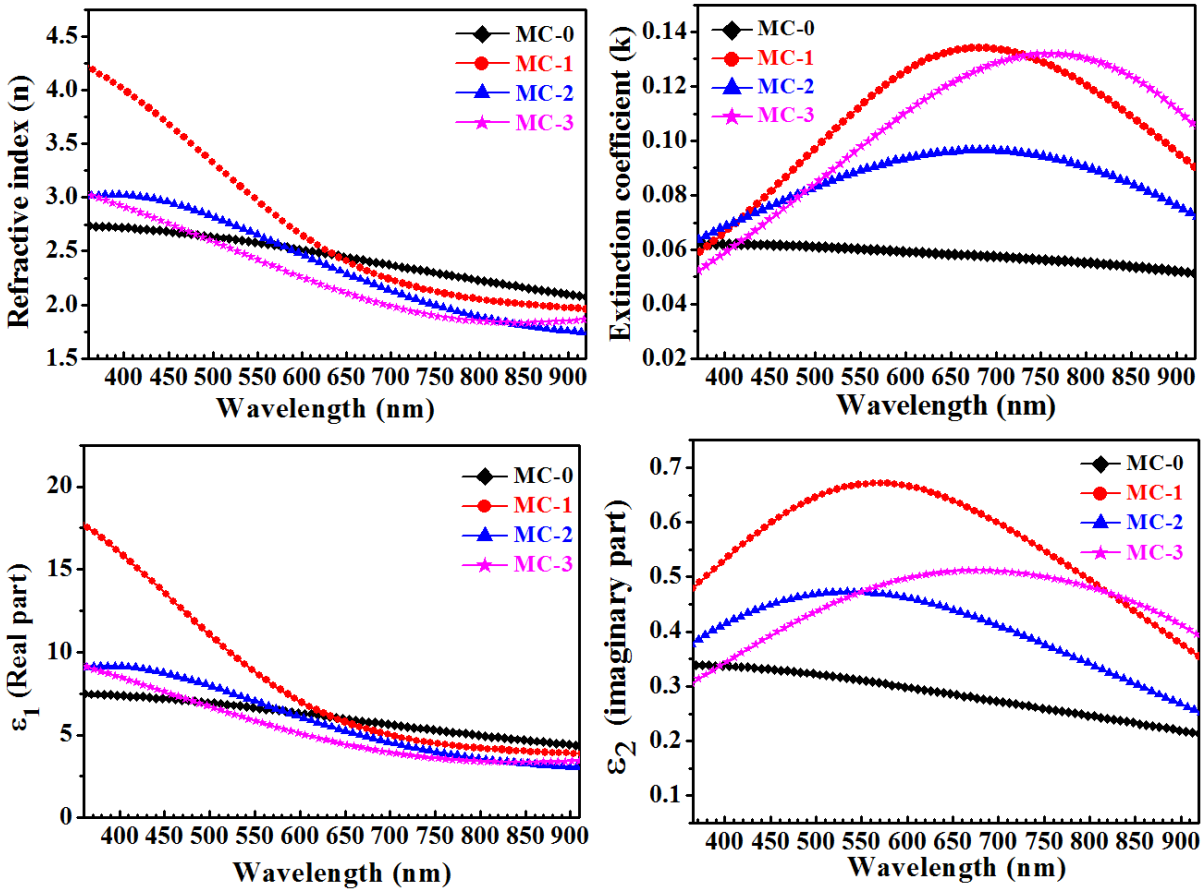
Refractive index (n)
Wavelength (nm)
MC-0
MC-1
MC-2
MC-3
Extinction coefficient (k)
Wavelength (nm)
MC-0
MC-1
MC-2
MC-3
ε1 (Real part)
Wavelength (nm)
MC-0
MC-1
MC-2
MC-3
ε2 (imaginary part)
Wavelength (nm)
MC-0
MC-1
MC-2
MC-3

Fig. 6

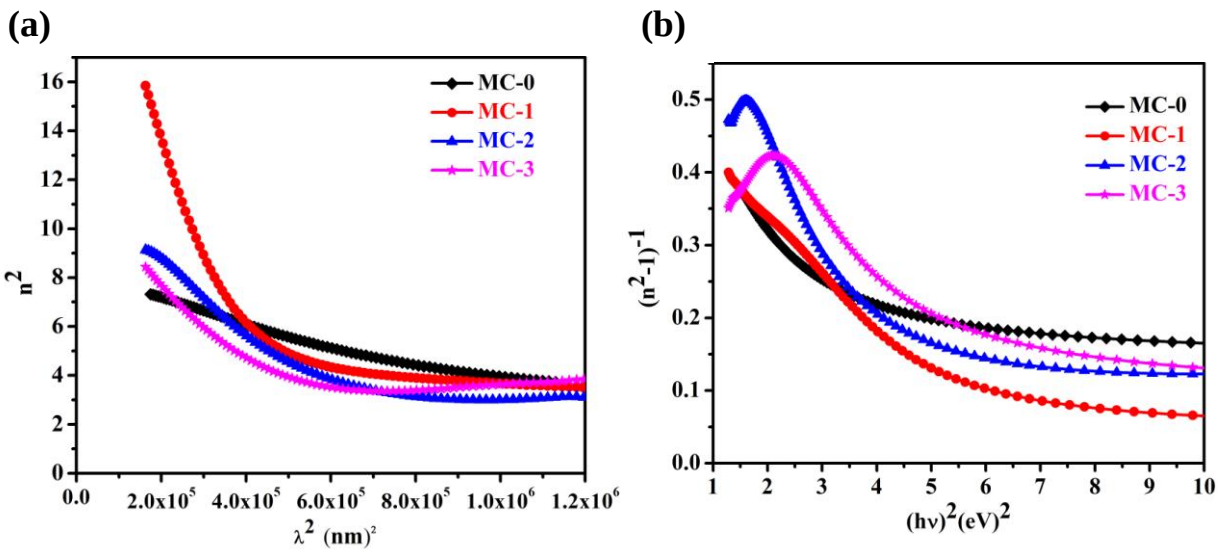

Fig. 7

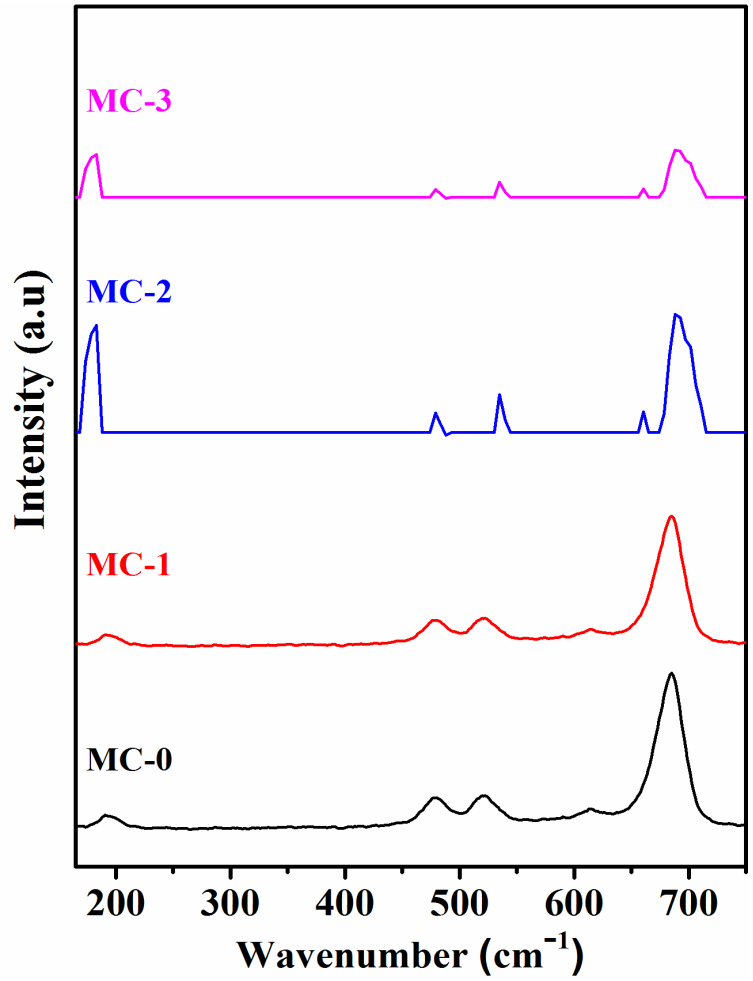
MC-3
MC-2
MC-1
MC-0
Intensity (a.u)
200
300
400
500
600
700
Wavenumber (cm-1)

Fig. 8

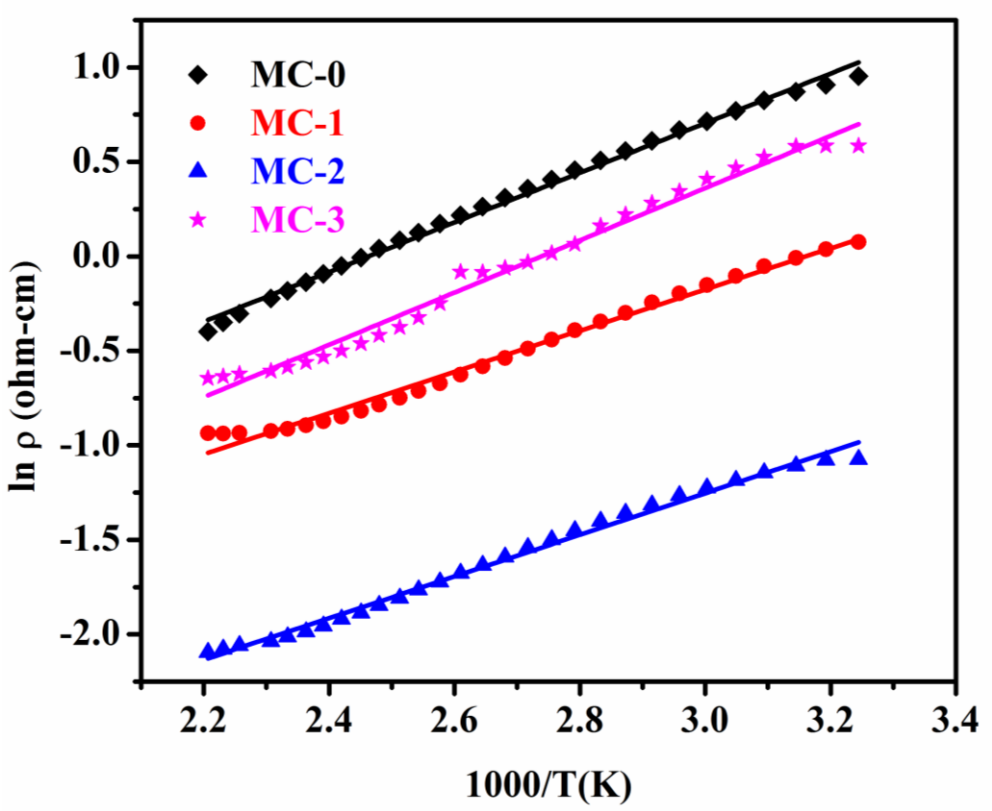
MC-0
MC-1
MC-2
MC-3
ln ρ (ohm-cm)
1000/T(K)
1.0
0.5
0.0
-0.5
-1.0
-1.5
-2.0
2.2
2.4
2.6
2.8
3.0
3.2
3.4

Fig. 9

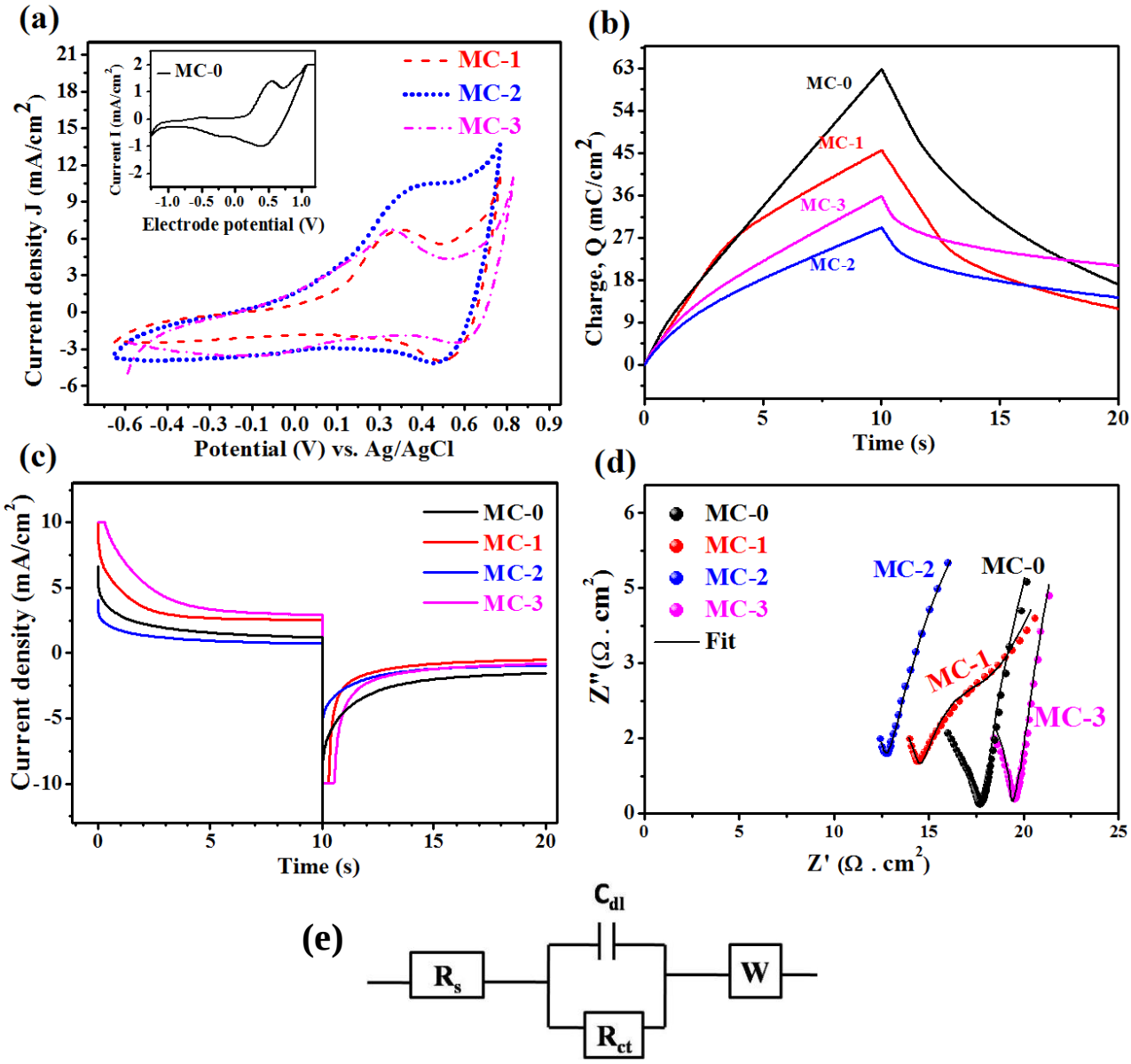
(a)
Current density J (mA/cm^2)
Potential (V) vs. Ag/AgCl
MC-1
MC-2
MC-3
MC-0
Current I (mA/cm^2)
Electrode potential (V)
(b)
Charge, Q (mC/cm^2)
Time (s)
MC-0
MC-1
MC-3
MC-2
(c)
Current density (mA/cm^2)
Time (s)
MC-0
MC-1
MC-2
MC-3
(d)
Z''(Ω . cm^2)
Z' (Ω . cm^2)
MC-0
MC-1
MC-2
MC-3
Fit
MC-2
MC-0
MC-1
MC-3
(e)
C_{dl}
R_s
R_{ct}
W

Fig. 10

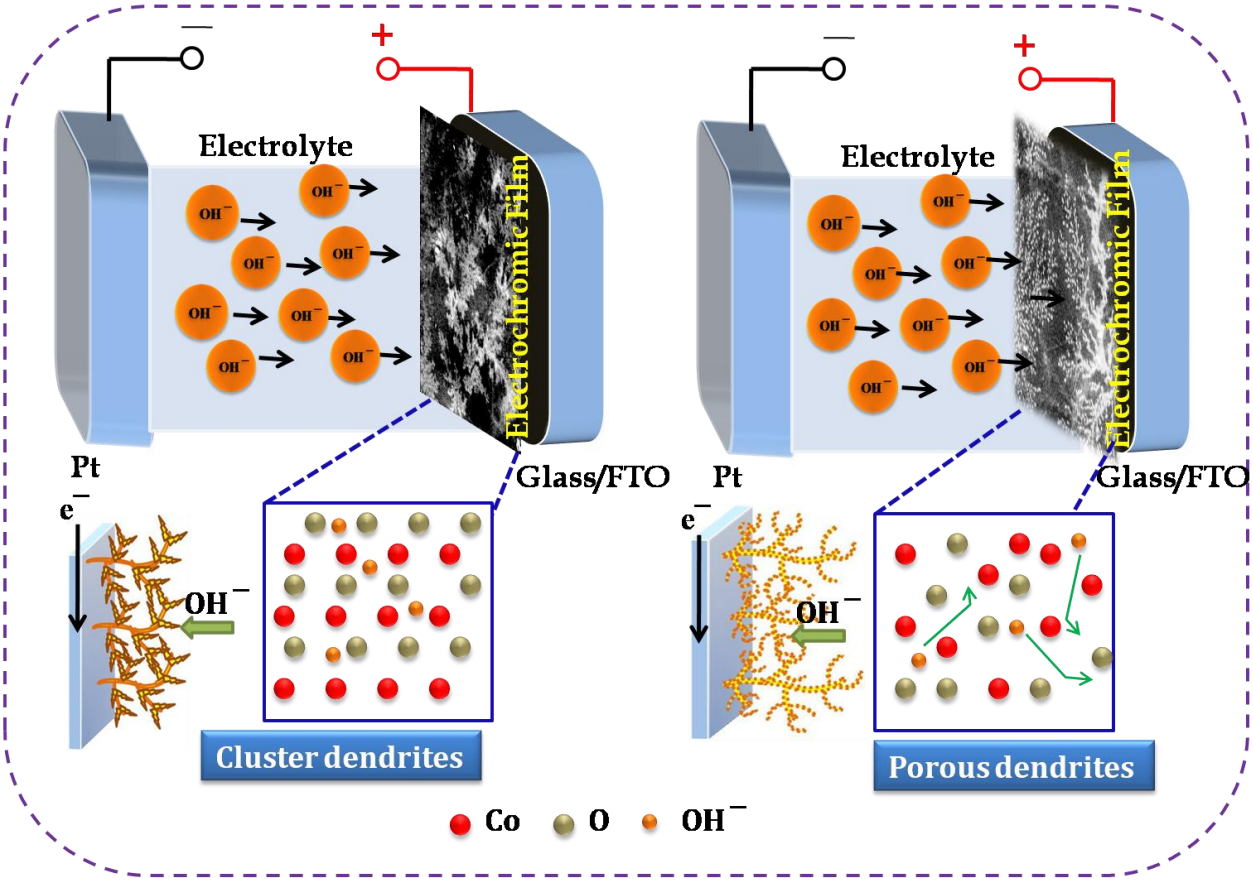
Electrolyte
Electrochromic Film
Glass/FTO
Pt
e⁻
OH⁻
Cluster dendrites
Porous dendrites
Co
O
OH⁻

Fig. 11

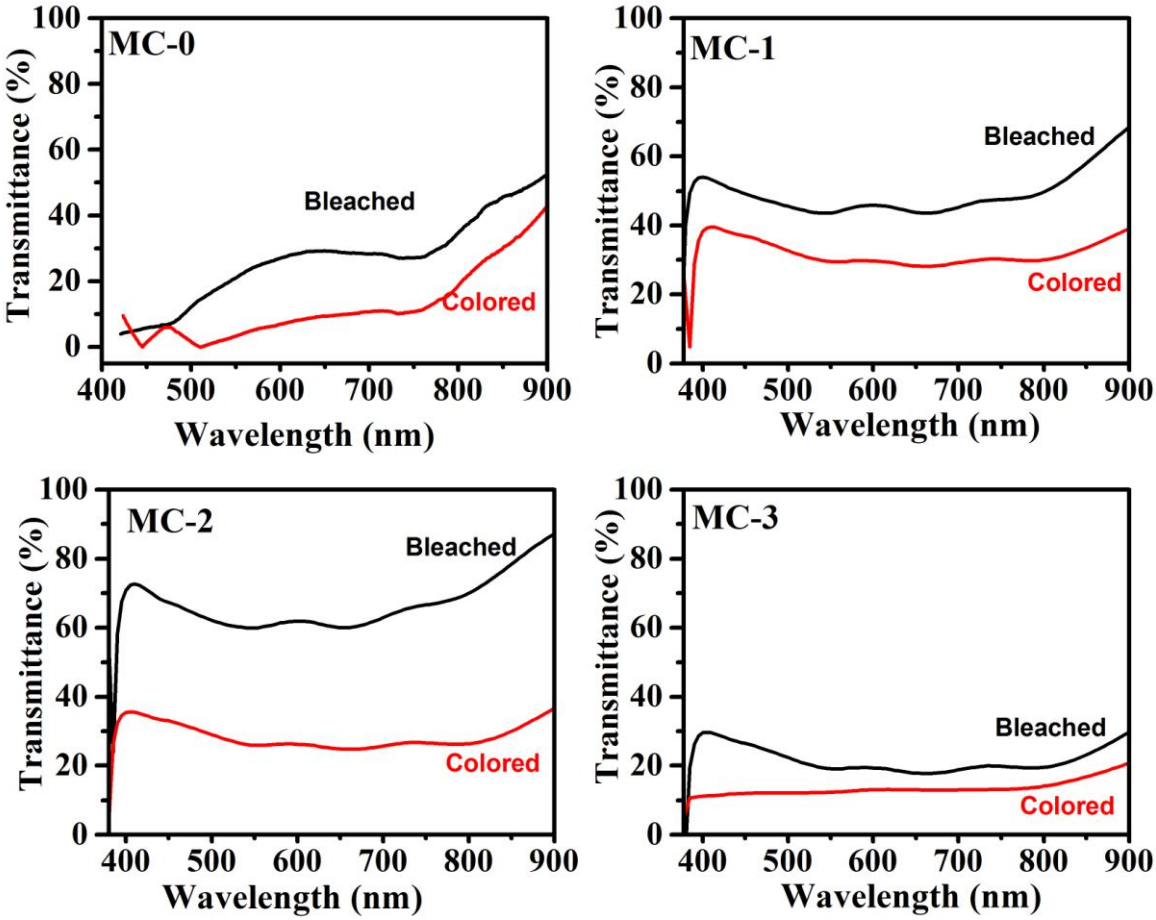
MC-0
Bleached
Colored
Transmittance (%)
Wavelength (nm)
MC-1
Bleached
Colored
Transmittance (%)
Wavelength (nm)
MC-2
Bleached
Colored
Transmittance (%)
Wavelength (nm)
MC-3
Bleached
Colored
Transmittance (%)
Wavelength (nm)

Fig. 12

Table 1

Sample	Crystallite Size D (nm)	Interplanar spacing d (Å)	Microstrain ε	Lattice parameter a (Å)	Unit cell Volume $(Å)^3$
MC-0	35	2.4391	9.7×10^{-4}	8.089	529.37
MC-1	18	2.4381	1.7×10^{-3}	8.083	528.10
MC-2	10	2.4348	3.4×10^{-3}	8.070	525.57
MC-3	14	2.4357	2.2×10^{-3}	8.079	527.31

* values calculated at predominant plane (311).

Table 2

Sample	Optical constants at λ=550 nm		(ε_L)	N/m*×10^{55} (cm^{-3}/g)	$\omega_p \times 10^{14}$ (s^{-1})	E_0 (eV)	E_d (eV)	n_0
	n	k						
MC-0	2.57	0.05	7.82	1.58	2.14	4.17	12.60	2.00
MC-1	2.99	0.12	10.27	2.16	2.49	4.12	9.73	1.93
MC-2	2.52	0.08	8.96	2.53	2.70	4.08	8.37	1.80
MC-3	2.68	0.10	8.12	1.93	2.36	3.92	9.44	1.84

Table 3

Sample	Sheet resistance R_{sh} (Ω/Sq.)	Resistivity ρ (Ω-cm)	Activation energy E_a (eV)
MC-0	9.1×10^3	2.59	0.52
MC-1	3.7×10^3	1.08	0.40
MC-2	1.2×10^3	0.34	0.38
MC-3	6.2×10^3	1.80	0.43

Table 4

Sample	E_{pc} (mV)	E_{pa} (mV)	J_{pa} (mA/cm^2)	J_{pc} (mA/cm^2)	Diffusion coefficient (D) ($cm^2\ s^{-1}$)	
					I_{pa}	I_{pc}
MC-0	540	450	1.46	0.99	1.94×10^{-15}	1.06×10^{-15}
MC-1	491	371	6.7	3.77	4.85×10^{-14}	1.54×10^{-14}
MC-2	468	403	10.1	4.13	1.10×10^{-13}	1.85×10^{-14}
MC-3	337	558	6.68	2.35	4.83×10^{-14}	6×10^{-14}

Table 5

Sample	Q_i (mC/cm^2)	Q_{di} (mC/cm^2)	Reversibility (%)	$Q_i - Q_{di}$ (mC/cm^2)
MC-0	64	49	76.5	15
MC-1	41	26.71	64.05	14.29
MC-2	29	23.95	82.58	8.05
MC-3	34	14.1	41.47	19.9

Table 6

Sample	Response time (s)		Transmittance (%)			PCR	Δ OD	CE (cm^2/C)
	t_b	t_c	T_b	T_c	Δ T			
MC-0	1.1	1.6	28.93	8.69	20.24	3.32	1.20	18.8
MC-1	2.3	1.5	44.13	24.22	20.03	1.82	0.59	15.0
MC-2	1.2	1.7	60.91	25.97	35.02	2.34	0.85	29.1
MC-3	3.9	3.2	18.92	13.32	5.6	1.42	0.35	10.3